Micromechanical modelling of ceramic based composites with statistically representative synthetic microstructures

P. Alveen[a,*], D. Carolan[a], D. McNamara[a], N. Murphy[a], A. Ivanković[a]

[a]*School of Mechanical and Materials Engineering, University College Dublin, Ireland*

Abstract

A combined experimental-numerical method was used to investigate the role of microstructure on the fracture of advanced ceramics. In particular, the effect of grain size and matrix content were examined. Two dimensional representative finite volume (FV) microstructures were created using Voronoi tessellation to synthetically represent the microstructure of a two phase ceramic composite. It is shown, by comparing with real micrographs, that the method captures the features of real microstructures in terms of grain size distribution, grain aspect ratio and the distribution of second phase agglomerations. Simulation results indicate the computed elastic parameters are within the Hashin-Shtrikman bounds and also agree well with the Eshelby-Mori-Tanaka method. It is found that the underlying microstructure significantly affects the local stress and strain distributions in these advanced ceramics.

Keywords: Advanced ceramics, microstructure, Voronoi tessellation, numerical model, image analysis, finite volume analysis

*Corresponding author

Email address: Patricia.Alveen@ucdconnect.ie (P. Alveen)

1. Introduction

Advanced ceramics are a class of material which exhibit superior properties to traditional ceramics, including abrasion resistance and high hardness. They are widely used as tool materials for the high speed machining of ferrous materials and other hard and abrasive materials, such as nickel-based super alloys [1]. They are well established for use in the automotive and aerospace industry [2] and are often used in extreme conditions involving high temperature and impact loading, which may lead to premature failure due to fracture or chipping. Therefore, it is desirable to understand the mechanisms which contribute to the failure of advanced ceramics in order to design improvements to the next generation of cutting tool materials.

The advanced ceramics in question have a two-phase ceramic structure composed of particles of a primary hard phase together with either a metallic or ceramic matrix material. Carolan et al [3, 4] have shown that the strength and toughness of these materials are affected by both the size of the primary phase and percentage matrix content. Therefore it is desirable to optimise these parameters to produce stronger or tougher materials for specific applications. Current methods adopt a so-called "trial-and-error" approach to the design of new materials, which is both costly and time consuming. Hence, it is beneficial to be able to specify improvements to materials numerically. By specifying materials virtually, the influence of individual material parameters on the microstructural scale can easily be investigated and altered to change bulk material properties. In order to better model and predict material behaviour, the first step is the ability to produce statistically representative

microstructures.

Certain microstructural properties such as grain size distribution, volume fraction and grain boundaries can be determined at high magnification from images obtained using scanning electron microscopes (SEM). Simple microstructures with large features are often analysed manually, however for multiple features with random shapes, such as micron sized grains in a microstructure, the human eye is prone to error [5]. Various manual methods may be used to increase the accuracy of the measurements [6], however this is still time consuming when measuring micron sized features, especially considering that some images can have upwards of several hundred grains. Therefore, automated image analysis is used to increase accuracy and reduce user effort. In the current work all the image analysis and processing routines were implemented in ImageJ [7] and MATLAB [8].

According to Groeber et al [9], early methods for microstructural modelling included the use of cubes, spheres and ellipsoids to represent real microstructures. It is well established that strength and toughness of ceramics are dependent on microstructure [10–12] and, as mentioned by Zhang et al [13], stress and strain are related to grain size, shape, orientation and distribution. Therefore it is important to ensure that the synthetic microstructures are representative of the real microstructures they were created to replace. This is especially important in the case of fracture problems, where the morphology of a grain or phase boundary is of added relevance in determining fracture initiation.

A number of authors [14–16] have generated 2D finite element meshes directly based on actual microstructural images which may be obtained using

various methods including SEM, Electron Backscatter Diffraction (EBSD) and x-ray tomography. Coffman et al [17] use serial sectioning and imaging of a material to obtain a real 3D microstructure and hence apply a finite element mesh to create a 3D model. These methods all require a microstructural image to produce a numerical model, which ensures that the finite element model is statistically representative of the real microstructure. However, this would not be possible in the case of virtual design of a new material.

Numerous studies have been carried out to produce numerical microstructures using Voronoi tessellation [18–20]. It is well established that polycrystalline microstructures can be modelled using Voronoi tessellations. Nygårds and Gudmundson [21] use Voronoi tessellations to create 3D geometrical models of 2-phase ferrite/pearlite steel with periodic boundary conditions. Kühn and Steinhauser [22] model polycrystalline materials using power diagrams which are a generalisation of Voronoi diagrams for arbitrary dimensions. Voronoi tessellations have also been used to investigate fracture of brittle materials. Espinosa and Zavattieri [23] investigate failure initiation in brittle materials, while Warner and Molinari [24] model compressive fracture of alumina ceramics. Zhou et al [25] have used Voronoi tessellations to investigate crack propagation in ceramic tool materials. Danielsson et al [26] have also investigated plasticity using Voronoi tessellations, by modelling elasto-viscoplastic deformation of rubber-toughened glassy polymers.

Zhang et al [13, 27] used a controlled Poisson Voronoi tessellation model to generate polycrystalline microstructures. They introduced control parameters to control the regularity of the microstructure and ensure that the grain size distribution is statistically equivalent to real microstructures. As men-

tioned previously this is important in the case of fracture problems where the microstructure morphology will affect fracture initiation. Saylor et al [28] use geometry and crystallographic observations to ensure that their numerical microstructures are statistically representative.

Nygårds and Gudmundson [21], Li et al [29] and Wang et al [30] have all created 2-phase microstructures using Voronoi tessellations. The present work attempts to create randomly distributed two-phase synthetic microstructures which are statistically representative of real ceramic microstructures. This will be achieved using a combined image analysis and Voronoi tessellation approach. The synthetic microstructures will then be used to investigate the role of microstructure on the stress and strain distributions within these ceramics.

2. Microstructural Analysis

Microstructural images of real microstructures were obtained via electron backscatter mode using a FEI Quanta 3D FEG DualBeam SEM. In order to analyse a microstructural image systematically, some processing of the image was required. Image enhancement is the process whereby the image quality is improved to define specific features and edges, without changing the total amount of data. Various image processing tools can be used to achieve this, such as filtering, increasing contrast and colour thresholding.

2.1. Image Processing

2.1.1. Thresholding

The process in which the grey-scale image is converted to a binary image is called thresholding. The goal of thresholding is to separate features so

that analysis, such as counting and measurement, can be carried out. This is achieved by selecting the grey-level range for the features of interest. It can be seen from the histogram, Figure 1a, that there is a feature of interest in the grey-scale range of 20-70. The pixels within this threshold level are assigned as the foreground and are given a value of 0. Everything else is assigned as the background and is given a value of 1. It should now be easy to distinguish the two phases, Figure 1c.

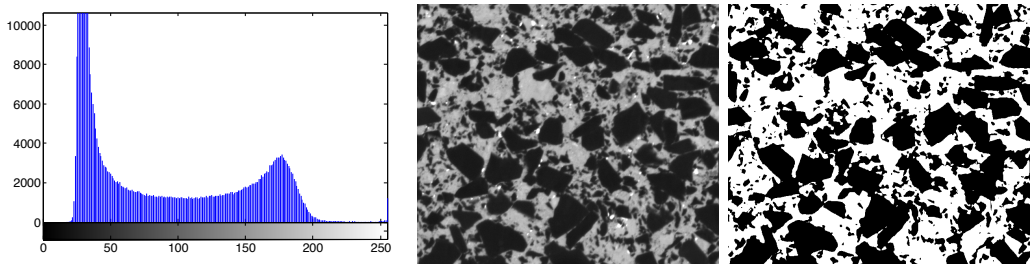

(a) Histogram of grey colour values (b) Original grey scale image (c) Binary Image

Figure 1: Original and threshold image of the ceramic microstructure, including histogram of the grey colour values, with the grains shown in black and the matrix in white

2.1.2. Watershed Segmentation

A difficulty that arises in the analysis of microstructural images is the problem of touching or overlapping grains. If two or more grains are touching, they will be seen as a single feature by the image analysis software. A common method used for segmenting touching features is the watershed segmentation method [31–34]. This is clearly demonstrated schematically in Figure 2. The binary image is converted into a Euclidean distance map, (2b), where each pixel intensity represents the distance of that pixel from an edge.

A contour plot of the Euclidean distance transform, (2c), is analogous to a geographic map of basins and valleys. The distance map is then eroded until only the lowest points remain. Finally, the image is dilated from these points at a constant velocity, known as flooding, and when two or more flooded basins meet a dam is built which is the watershed line, (2d), [35]. The watershed segmentation process for an advanced ceramic microstructure can be seen in Figure 3.

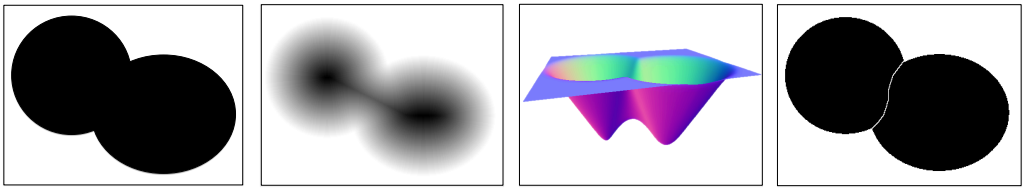

(a) Original image (b) Euclidean distance map (c) Contour plot (d) Segmented image

Figure 2: Schematic representation of the watershed segmentation process

2.2. Image Analysis

Individual grains in the microstructure can be analysed using the segmented image. The sintering process causes small fragments of grains to be scattered throughout the matrix material. These small fragments were excluded due to computational reasons, as they would significantly increase the computational time and cause meshing difficulties. Secondly, previous research by our group [3] has shown that the critical length scale of these types of materials is of the order of the particulate grain size. Therefore, it is not thought that these small fragments significantly affect the overall material property. The percentage of each phase was also determined by obtaining the ratio of black to white pixels in the binary image. This corresponds to

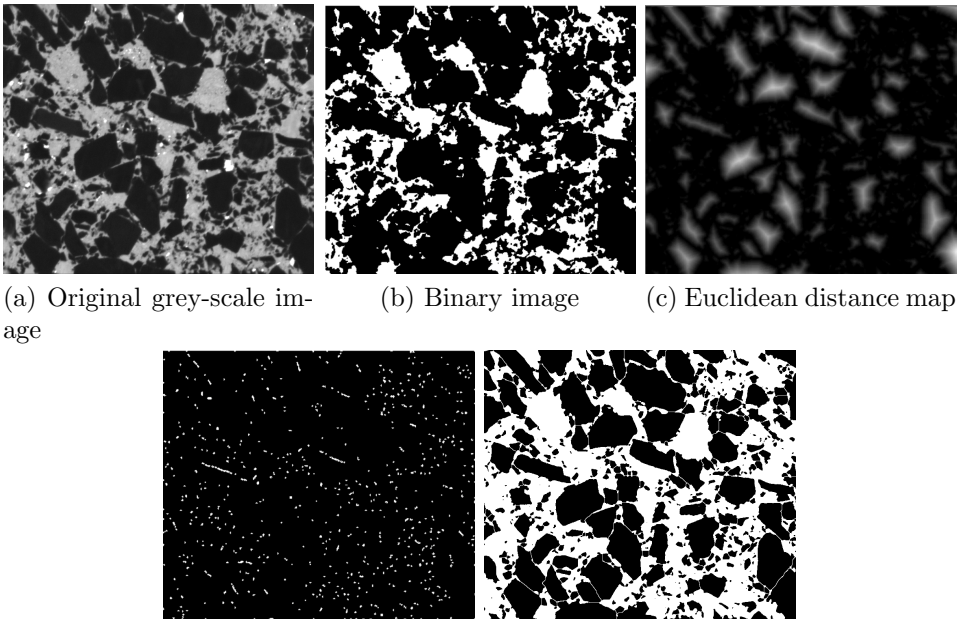

(a) Original grey-scale image (b) Binary image (c) Euclidean distance map

(d) Ultimate eroded points (e) Segmented image

Figure 3: Watershed segmentation sequence starting from the original grey-scale image (a), converting this to a binary image (b), getting the Euclidean distance map (c), eroding this image to get the ultimate eroded points which are used as markers (d), and then the final segmented image (e)

the area fraction which has been shown to be equal to the volume fraction [36].

Grains along the image borders cause inaccuracies in both the number of grains and their corresponding size distribution. When grains intersect the image border, their full size is not accounted for. Furthermore, larger grains are more likely to intersect the image border; so completely excluding border grains would further affect the accuracy of the size distribution. According to Russ [6] a simple method to account for this is to exclude grains that touch two adjacent borders, for example bottom and right, but include the grains that touch the remaining borders.

2.3. Aspect Ratio

A measure of grain shape is provided by considering the aspect ratio of each grain. Aspect ratio is the ratio of the minor axis length, b, to the major axis length, a, of the bounding ellipse. For irregular polygon shapes, such as grains, the major and minor axis lengths are found using the normalised second central moment. The second central moment, also called the variance, is a numerical measure of how the data values are dispersed around the mean. The k^{th} central moment of a data sample is found using Equation 1, where k is the order, N is the sample size, p is the data set and $\bar{p}$ is the mean value, or in the case of grain coordinates the centroid. For the normalised second central moment $1/12$ is added for a pixel with unit length [8].

$$m_k = \frac{1}{N}\sum_{i=1}^{N}(p_i - \bar{p})^k \tag{1}$$

The three second central moments of interest for the current work are given in Equations 2, 3 and 4.

$$m_{xx,i} = \frac{1}{N}\sum_{i=1}^{N}(x_i - \bar{x_i})^2 + \frac{1}{12} \tag{2}$$

$$m_{yy,i} = \frac{1}{N}\sum_{i=1}^{N}(y_i - \bar{y_i})^2 + \frac{1}{12} \tag{3}$$

$$m_{xy,i} = \frac{1}{N}\sum_{i=1}^{N}(x_i - \bar{x})(y_i - \bar{y_i}) \tag{4}$$

The second central moment of each grain is then used to calculate an

ellipse with the same normalised second central moment, see Figure 4. The major and minor axis lengths of these ellipses are then calculated using Equations 5 and 6 [37], which then are used to calculate the aspect ratio.

$$a = 2\sqrt{2}\sqrt{m_{xx} + m_{yy} + \sqrt{(m_{xx} - m_{yy})^2 + 4m_{xy}^2}} \tag{5}$$

$$b = 2\sqrt{2}\sqrt{m_{xx} + m_{yy} - \sqrt{(m_{xx} - m_{yy})^2 + 4m_{xy}^2}} \tag{6}$$

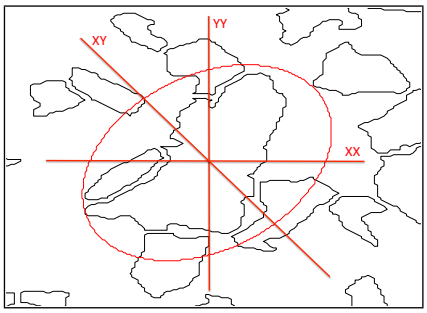

Figure 4: Image showing fitting of ellipses with same second central moment to microstructure

2.4. k-Nearest Neighbour Distance

Nearest neighbours can be used as a measure of spacial arrangement to describe microstructural features, such as particles or voids. Given a point, X, and a data set, Y, the k-nearest neighbour search finds the k nearest neighbours in Y to the point X, where k is a positive integer, and measures the distance between this point and the neighbours, see Figure 5. The k-nearest neighbour search uses a k-d tree to find the nearest neighbours, while the distance is measured using Euclidean distance. A k-d tree is a data structure

for organising points in a k-dimensional space [38]. For the purpose of the current work, the nearest neighbour distance was measured as the distance between centroids

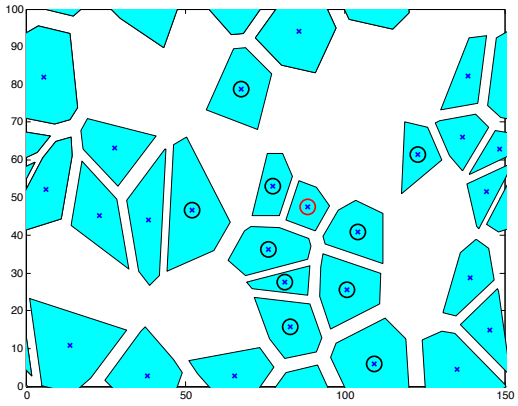

Figure 5: Image illustrating the 10 nearest neighbours, marked with a black 'O', to a specified point, marked with a red 'O'

2.5. Matrix Agglomerations

An important microstructural property when describing the two phase microstructures is the presence of matrix agglomerations (MA). It may be observed, when viewing images of microstructures, that there are often regions filled predominantly with the second-phase matrix material, see Figure 6. In the current work these regions are referred to as matrix agglomerations. Matrix agglomerations are found by carrying out morphological processing on the binary image until only the matrix agglomerations remain. An estimate of the percentage matrix agglomerations in the microstructure can then be obtained.

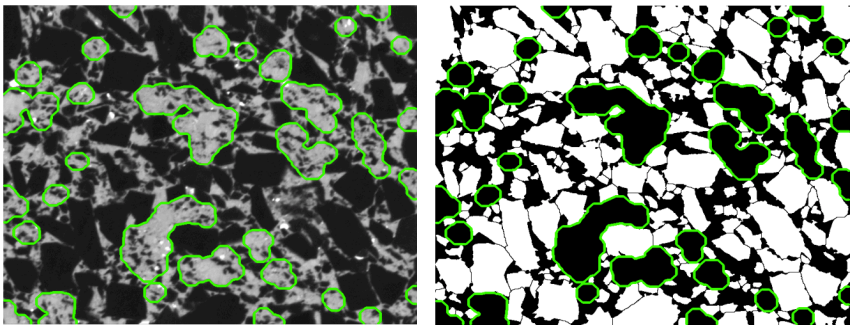

Figure 6: Grey-scale and binary image of a true microstructure with matrix agglomerations highlighted

3. Synthetic Microstructure Generation

Voronoi tessellation was used to generate the geometrical model of the microstructure. It is a commonly used method for the generation of numerical microstructures of ceramic and metallic materials in both two- and three-dimensions. The Voronoi tessellation algorithm produces a random structure which is representative of a polycrystalline material. The procedure for obtaining the numerical microstructure can be broken into three main steps:

- Generation of random seed points
- Voronoi tessellation to obtain the geometry
- Contraction of Voronoi elements to produce dual-phase microstructure

3.1. Voronoi Tessellation

Consider a pair of seed points, a and b, in $\mathbb{R}^2$ as shown in Figure 7. The perpendicular bisector of ab divides the plane into two halves. All points in the plane on one side of the perpendicular bisector are closer to a than

to b, while all points on the opposite side of the perpendicular bisector are closer to b than to a. Next consider a third seed point, c. The perpendicular bisectors of ac and bc can be drawn as before. There are now three regions surrounding each seed point. Each region coincides at the circumcentre of abc. Repeating this procedure, for other seed points divides $\mathbb{R}^2$ into a series of polygons known as a Voronoi diagram. A typical Voronoi Tessellation with 100 random seed points distributed randomly on the region $0 < x, y < 1$ is given in Figure 8. As Voronoi tessellation is defined on the entire plane, special care has to be taken with any seed points close to the boundary which do not have sufficient neighbours to define a closed polygon. In the current work, periodicity of the microstructure is enforced by copying the seed points in the region of interest to the eight adjoining rectangles and applying the tessellation procedure to the larger domain. Finally, the tessellation in the region of interest is extracted for further processing.

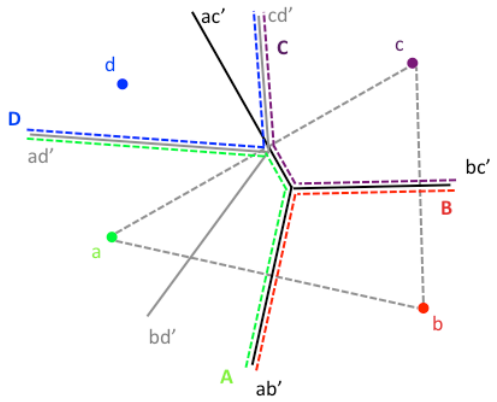

Figure 7: Schematic showing the Voronoi tessellation of $\mathbb{R}^2$ by four seed points. The area A indicates that part of $\mathbb{R}^2$ which is closer to a than to either b, c, or d.

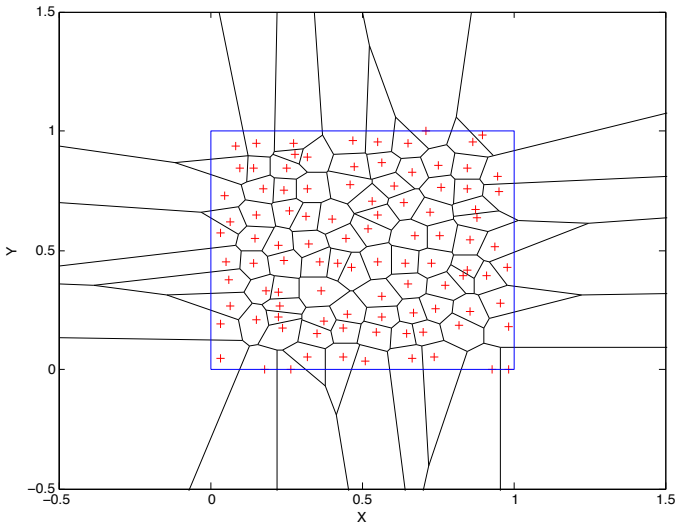

Figure 8: Open Voronoi tessellation on the region $0 < x, y < 1$.

In order to study the effect of grain size and microstructure, Voronoi tessellation is used to generate random microstructures of a ceramic based composite. First, the boundaries of the solution domain are specified. The required number of seeds is then distributed uniformly throughout the domain. A degree of irregularity in the microstructure is then introduced by allowing the seeds to migrate from their initial positions according to a bounded random distribution. The degree of displacement of the seed points is controlled by two random variables, a distance r, which is normally distributed, and an angle θ, which is uniformly distributed between 0 and 2 π. The distance r represents the magnitude of the vector connecting the positions of the initial and final seed points, while the angle θ gives the direction of this vector with $\theta = 0$ being the positive direction of the abscissa. The user determines the standard deviation of the distance parameter r. An upper bound on the allowable value of r can also be imposed. This prevents the seeds from

moving too close to one another and, subsequently, producing a microstructure which is physically unrealistic. The effect of regularity on the generated microstructure is shown in Figure 9.

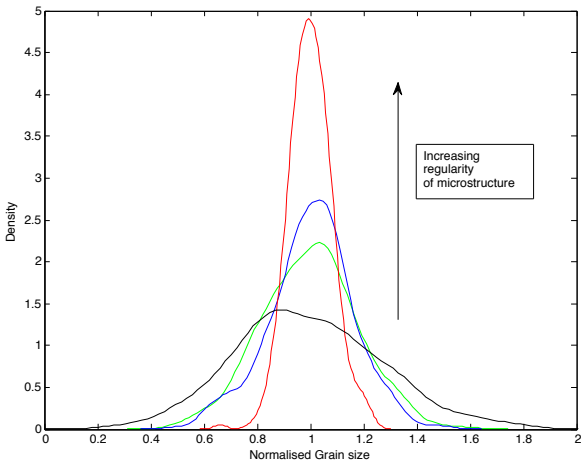

(a) Density, where the highest density distribution corresponds to (b) and lowest corresponds to (c)

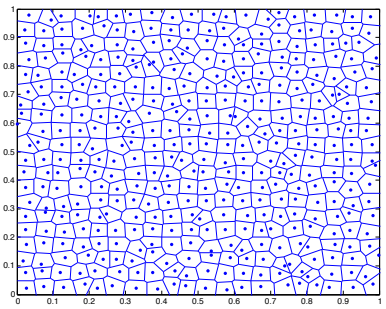

(b) A regular microstructure on a 1 by 1 grid.

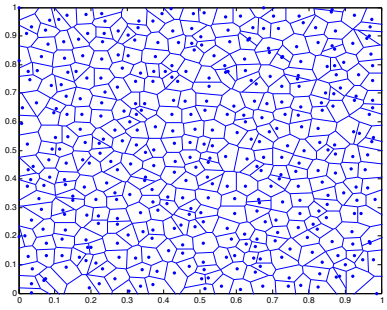

(c) An irregular microstructure on a 1 by 1 grid.

Figure 9: Effect of regularity on the grain size distribution of the final microstructure.

3.2. Numerical Microstructure

To generate a dual interpenetrating phase microstructure, typical of advanced ceramics, the Voronoi tessellation is applied as before. Each Voronoi tile is then reduced in area around the circumcentre of the tile until the desired area fraction of the second interpenetrating phase is reached. To create a statistically representative microstructure the area fraction is set equal to the percentage grains obtained during the image analysis of the true microstructures. Another important aspect of the ceramic microstructure is the matrix agglomerations. In order to obtain matrix agglomerations in the microstructure, a specified number of grains are removed from the microstructure, keeping the specified particle phase content constant, as shown in Figure 10.

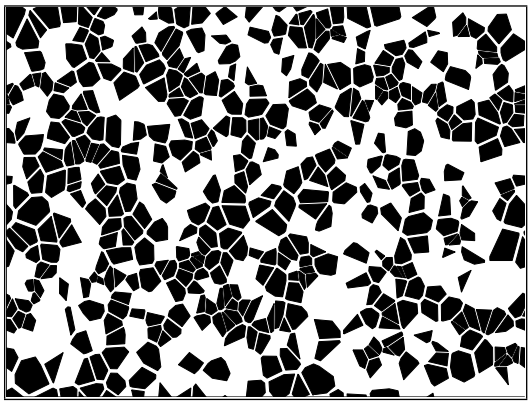

Figure 10: Numerical ceramic microstructure with 50% particulates and matrix agglomerations

4. Results

4.1. Comparison of real and numerical microstructures

It was found, using image analysis, that a real microstructure had an average particle content of 46.1%. A synthetic microstructure was generated for comparison, see Figure 11b. The generated microstructure had a particle content of 47%. The percentage matrix agglomerations with respect to grain content for the real microstructure was found to have an average value of 55.4%, while the synthetic microstructures had matrix agglomerations of 58%.

Grain size distribution, average k-nearest neighbour distance and aspect ratio were obtained for both the numerical and the real microstructure. A comparison between the two confirms that the numerical model is a good representation of the real microstructure, see Figures 11a and 11b. The grain size distribution of both the real and the numerical microstructure follow a log-normal distribution with a greater number of small grains, see Figure 11c. The real microstructure has a higher percentage of these small grains than its numerical counterpart due to the small fragmented grains. It can be seen that from Figure 11d there is very good agreement between the average nearest neighbour distances of the real and the numerical microstructures. The aspect ratio of the real and the numerical microstructures also show excellent agreement, as shown in Figure 11e. Visually it is also observed that there is a good correlation between the numerical microstructure and the real microstructure.

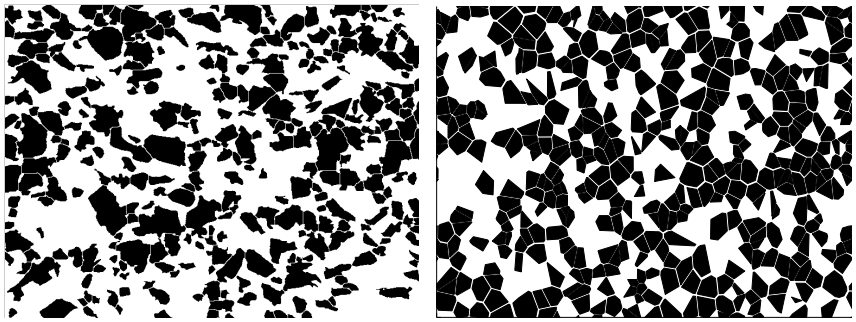

(a) Real microstructure (b) Numerical microstructure

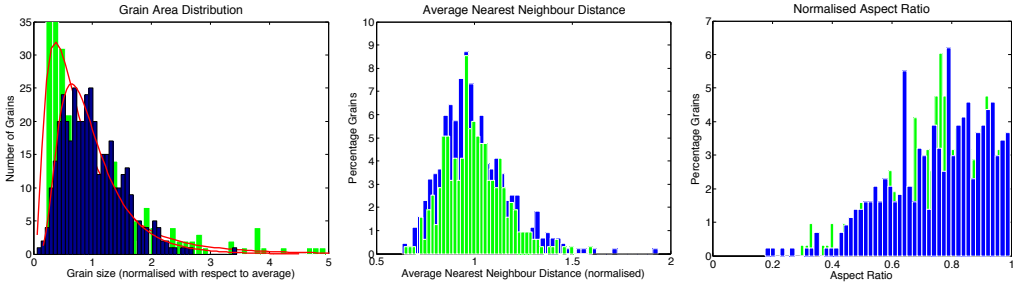

(c) Grain size distribution (d) Nearest neighbour distance (e) Aspect ratio

Figure 11: Comparison of (a) real and (b) numerical microstructures in terms of (c) grain size distribution, (d) nearest neighbour distance and (e) aspect ratio, with real shown in green and numerical in blue.

4.2. Finite Volume Analysis

Finite volume based stress analysis was carried out on six generated microstructures using OpenFOAM 1.6-ext [39]. Each generated microstructure was $100\times100\mu$m in size with approximately 40%, 50% and 60% grains, but with varying grain sizes, as shown in Figure 12. In addition, two microstructures with 50% grains and matrix agglomerations, shown in Figure 12d and 12h, were also tested to investigate the effect of matrix agglomerations.

The simulations were 2-dimensional and plane strain was specified in the third direction. Both the particulates and matrix were treated as isotropic

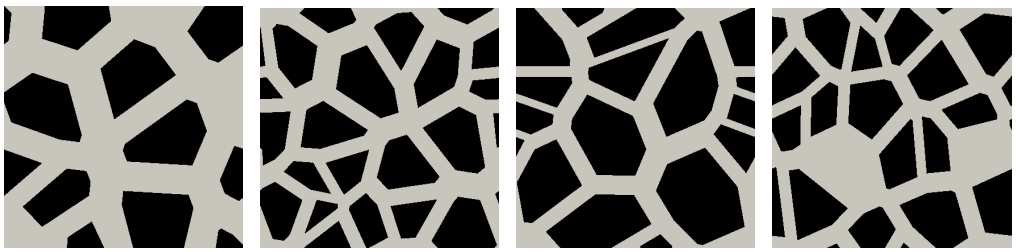

(a) 5x5 grains with 40% grains

(b) 5x5 grains with 50% grains

(c) 5x5 grains with 60% grains

(d) 5x5 grains with 50% grains and MA

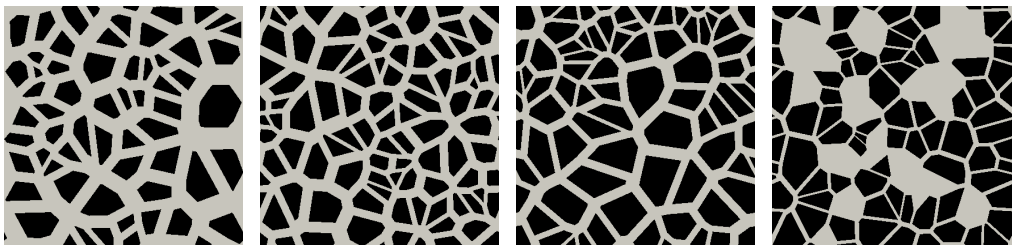

(e) 10x10 grains with 40% grains

(f) 10x10 grains with 50% grains

(g) 10x10 grains with 60% grains

(h) 10x10 grains with 50% grains and MA

Figure 12: Numerical microstructures used for finite volume analysis

linear elastic over the course of the simulation. The Young's modulus and Poisson's ratio are as shown in Table 1. It should be noted that the elastic constants of each phase are not representative of any particular material. The microstructures were subjected to a normal traction rate of 10 MPa/s in the positive y-direction for a total loading time of 10 seconds, while periodic boundary conditions were applied in the x-direction, see Figure 13. The

	E [GPa]	ν
Primary Phase	800	0.1
Secondary Phase	300	0.1

Table 1: Material properties

periodic boundary conditions ensure that both materials and displacement distribution are continuous from right to left. This avoids any undesirable edge effects due to skew elements at the boundary.

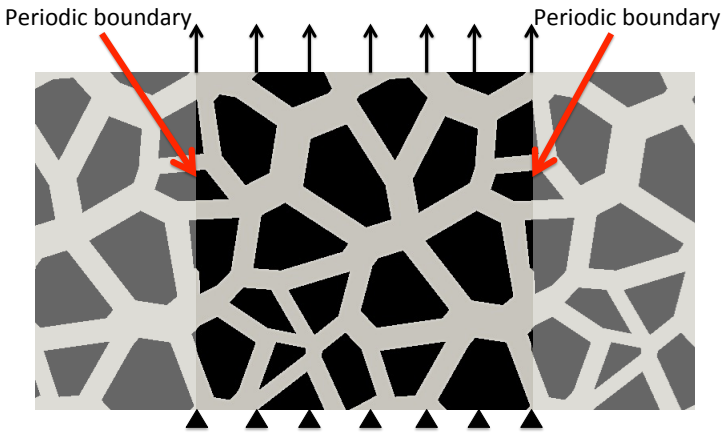

Figure 13: Generated microstructure with periodic boundary conditions subjected to a fixed traction

4.3. Effective elastic properties

The Young's Modulus value of a multiphase material depends on the properties of the individual phases. The upper and lower bounds for the elastic properties of the microstructures can be found using the Hashin-Shtrikman method from Equations 7 and 8. The Hashin-Shtrikman bounds can be applied to transversely isotropic composites with arbitrary phase geometry [40–42].

$$k_l = k_2 + \frac{m_1}{\frac{1}{k_1 - k_2} + \frac{m_2}{k_2 + \mu_2}}, \quad k_u = k_1 + \frac{m_2}{\frac{1}{k_2 - k_1} + \frac{m_1}{k_1 + \mu_1}} \tag{7}$$

$$\mu_l = \mu_2 + \frac{m_1}{\frac{1}{\mu_1 - \mu_2} + \frac{m_2(k_2 + 2\mu_2)}{2\mu_2(k_2 + \mu_2)}}, \quad \mu_u = \mu_1 + \frac{m_2}{\frac{1}{\mu_2 - \mu_1} + \frac{m_1(k_1 + 2\mu_1)}{2\mu_1(k_1 + \mu_1)}} \tag{8}$$

Where l and u represent the upper and lower bounds respectively, k is the bulk modulus, μ is the shear modulus, m is the volume fraction and 1 and 2 represent the two phases in the material.

$$E = \frac{9k_i\mu_i}{3k_i + \mu_i} \tag{9}$$

$$\nu = \frac{3k_i - 2\mu_i}{6k_i + 2\mu_i} \tag{10}$$

The upper and lower bounds for the Young's modulus and Poisson's ratio can then be calculated from Equations 9 and 10 respectively [29], by letting i equal to u and l from Equations 7 and 8. Using the Hashin-Shtrikman method the Young's modulus bounds are shown Table 2.

The Eshelby-Mori-Tanaka approach [43–45] for determining the elastic properties of composites containing randomly oriented inclusions was also employed in the current work. Using this approach, and treating the inclusions as circular, i.e. an aspect ratio of one, the ratio of bulk modulus, k, and shear modulus, μ of a composite material to that of the matrix can be written as:

$$\frac{k}{k_m} = \frac{1}{1 + V_f p} \tag{11}$$

$$\frac{\mu}{\mu_m} = \frac{1}{1 + V_f q} \tag{12}$$

where k_m, μ_m and V_f are the bulk modulus, shear modulus of the matrix and volume fraction of the inclusion respectively, and p and q are parameters

derived from the Eshelby tensor and defined in Tandon and Weng [43].

The effective stress, σ^e, and strain, ϵ^e, were found by averaging the local stress and strain in each cell using Equations 13 and 14 [46]. This is known as homogenisation.

$$\sigma^e = \frac{1}{V_\Omega} \int_{V_\Omega} \sigma dV \tag{13}$$

$$\epsilon^e = \frac{1}{V_\Omega} \int_{V_\Omega} \epsilon dV \tag{14}$$

Where V_Ω is the total volume of integration. These values were then used to calculate the effective Young's Modulus E^e from

$$E^e = \frac{1}{\epsilon^e_{yy}} [\sigma^e_{yy} - \nu^e(\sigma^e_{xx} + \sigma^e_{zz})] \tag{15}$$

where the effective Poisson's ratio, ν^e, is

$$\nu^e = \frac{\sigma^e_{xx}}{\sigma^e_{yy} + \sigma^e_{zz}} \tag{16}$$

The effective Young's modulus, $E_{Eq.15}$ of the microstructures is as shown in Table 2. The Young's modulus was also determined by calculating the average tractions and displacements on the loading boundaries. Using these values the stress, σ, and strain, ϵ, and hence the Young's Modulus, E, could be calculated by:

$$\sigma^e = \frac{F_1}{L_1} \tag{17}$$

$$\epsilon^e = \frac{u_1}{L_2} \tag{18}$$

$$E^e = \frac{\sigma^e}{\epsilon^e} \tag{19}$$

Where F_1 is the load per unit thickness on the prescribed boundary, L_1 and L_2 are the width and height of the specimen and u_1 is the displacement of the sample along the loading direction. The Young's modulus value calculated using Equation 19, was found to be higher than the value calculated using the homogenisation approach, see Table 2.

Microstructure	V_f	E_{HOM} **[GPa]**	E_{LD} **[GPa]**	E_{EMT} **[GPa]**	E_{HS} **[GPa]**
5×5	0.41	423.8	435.2	423.5	421.4-439.6
5×5	0.5	465.1	477.8	462.5	460.0-481.1
5×5	0.6	510.8	524.8	508.6	505.8-528.8
10×10	0.4	421.7	433.4	421.1	419.5-437.5
10×10	0.5	464.8	477.8	462.1	459.6-480.6
10×10	0.6	507.6	522.3	509.1	506.3-480.6
5×5 with MA	0.49	462.9	475.6	457.7	455.3-476.1
10×10 with MA	0.54	487.0	500.4	484.7	477.4-499.7

Table 2: Elastic properties of numerical microstructures where E_{HOM} is calculated using the homogenisation method in Eq.15, E_{LD} is calculated using the load-displacement method in Eq. 19, E_{EMT} is calculated using the Eshelby-Mori-Tanaka method, and E_{HS} is calculated using the Hashin-Shtrikman method

The Young's modulus value for the 5×5 and 10×10 microstructures with the same volume fraction of grains and no matrix agglomerations were found to be very similar using all the methods for calculating the Young's modulus. Furthermore, the Young's modulus values were only affected by the volume fraction of the phases and not by the presence of matrix agglomerations.

It was found that the load-displacement method consistently gave higher results than both the Eshelby-Mori-Tanaka and the homogenisation methods. The load-displacement values were found to lie close to the upper bounds of the Hashin-Shtrikman limits. The homogenisation was found to give realistic values for Young's modulus and these values were found to be in good

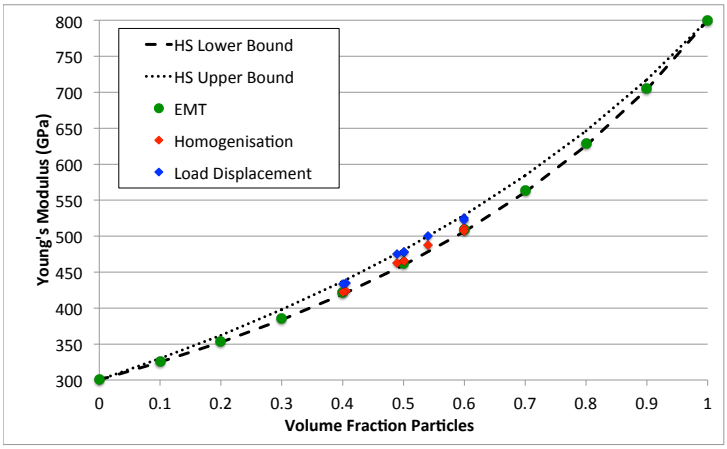

Figure 14: Graph of elastic properties versus particle content, where HS is the Hashin-Shtrikman bounds and EMT is the Eshelby-Mori-Tanaka method

agreement with the Eshelby-Mori-Tanaka method. Both these values tend to lie close to the lower bound of the Hashin-Shtrikman limits. This can be clearly seen in Figure 14

Figure 15 plots the distribution of Von-Mises equivalent stress for both the 5×5 and 10×10 microstructures with 40%, 50% and 60% grains. Similarly Figure 16 plots the distribution of Von-Mises equivalent strain for both the 5×5 and 10×10 microstructures. It may be observed that the distribution of local stress and strain does not vary significantly between the 5×5 and 10×10 microstructures with the same grain content. This would suggest that the local stress and strain distribution are not dependent on grain size.

The highest stresses were seen in the grains, while the highest strains were seen in the matrix material. Furthermore, it was noted that the microstructure with 40% particles had larger regions of high stress and strain and decreased as the particle content increased. This would suggest that as the particle content increases more of the strain is dispersed in the harder

phase. Hence, as particle content increases, the material strength is also expected to increase.

Figures 17 plot the distribution of Von-Mises equivalent stress and strain for the 5×5 and 10×10 microstructure with 50% grains and matrix agglomerations. When comparing the 5×5 and 10×10 microstructure with 50% grains from Figure 15 and 16 with Figure 17, it can be observed that the matrix agglomerations do affect the local distribution of stress and strain in the microstructure, with higher peak stresses and strains being observed. These peak stresses and strains are detected near the matrix agglomerations. The highest stresses are seen in the hard phase at the phase interface, while the highest strains are seen in the more compliant matrix phase. This demonstrates clearly that matrix agglomerations in the microstructure act as stress concentration factors.

5. Conclusion

The purpose of this paper was to develop statistically representative numerical models of advanced ceramic microstructures. The microstructures were generated using the Voronoi tessellation algorithm and subsequently altered to add a specified percentage particulates and matrix agglomerations to the microstructure. In the current paper it has been shown that the Voronoi Tessellation technique is a good method for the production of synthetic microstructures. The synthetic microstructures were compared to true microstructures and were found to be statistically representative in terms of grain size distribution, aspect ratio, average nearest neighbour distance and agglomeration of a second phase material.

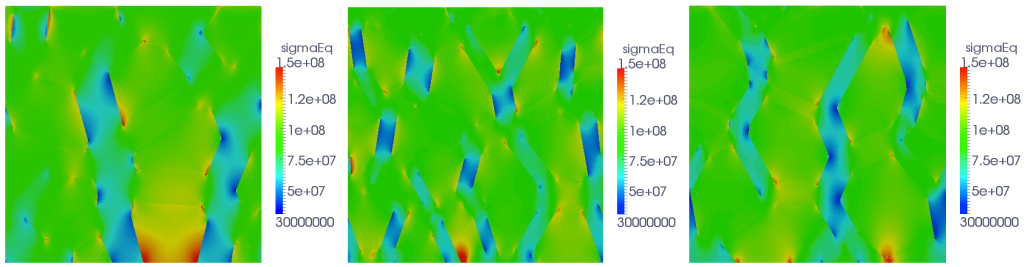

(a) 5x5 40% stress (b) 5x5 50% stress (c) 5x5 60% stress

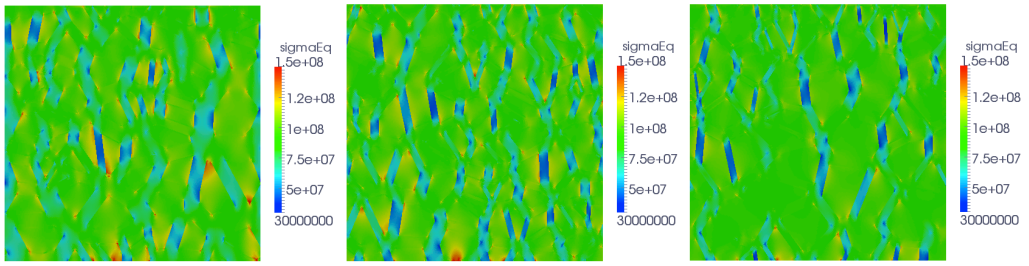

(d) 10x10 40% stress (e) 10x10 50% stress (f) 10x10 60% stress

Figure 15: Stress distribution in the numerical microstructures with no matrix agglomerations subjected to a normal traction.

Finite volume based stress analysis was carried out on a number of synthetic microstructures. The stress and strain distribution in the synthetic microstructures was calculated. Hence, the effective Young's modulus and Poisson's ratio were calculated. It was observed that the higher strains occur in the more compliant second phase material, which was more prevalent when there were agglomerations of the second phase material. Furthermore, it was observed that the presence of matrix agglomerations act as a stress concentration factor. Hence, the region surrounding the particulate matrix agglomeration interface is likely to be a potential source of failure for an in-service component. This emphasises the need for accurate representation of microstructures in a numerical model

It has been determined that the Young's modulus is dependent only on

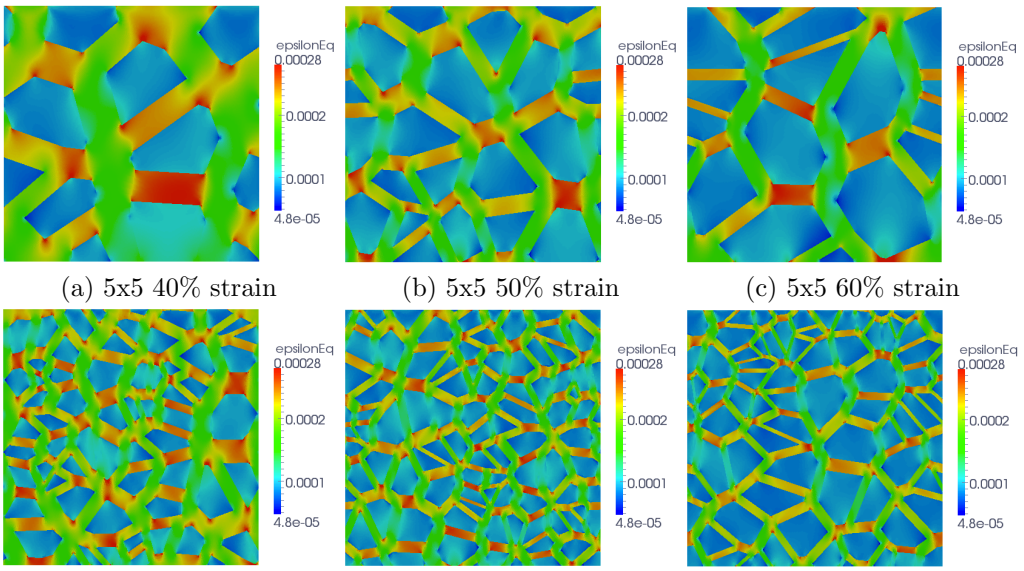

(a) 5x5 40% strain (b) 5x5 50% strain (c) 5x5 60% strain

(d) 10x10 40% strain (e) 10x10 50% strain (f) 10x10 60% strain

Figure 16: Strain distribution in the numerical microstructures with no matrix agglomerations subjected to a normal traction.

the volume fraction of the individual phases and not on the local distribution of those phases within a representative volume element. The Young's modulus of materials with both matrix phase agglomeration and no matrix phase agglomeration are not significantly different and agree closely with the predictions of Eshelby-Mori-Tanka approach.

The current paper presents a useful and implementable tool for investigating the effect of microstructural parameters on the microscopic stress distribution in a polycrystalline material.

6. Acknowledgements

The authors would like to thank Element Six Ltd., Enterprise Ireland and the Irish Research Council for providing financial support for this research.

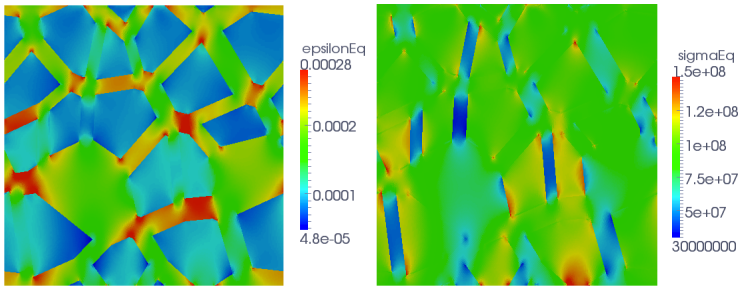

(a) 5x5 grains strain (b) 5x5 grains stress

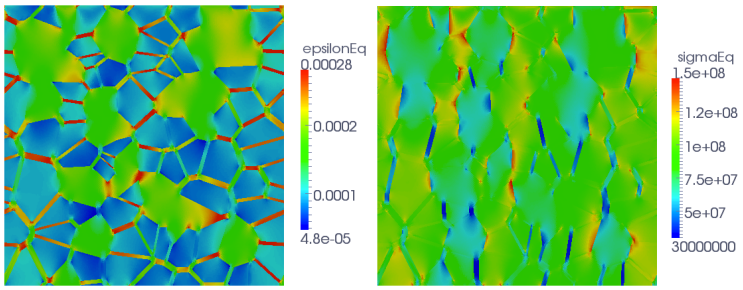

(c) 10x10 grains strain (d) 10x10 grains stress

Figure 17: Strain and stress distribution in the numerical microstructures with 50% grains and matrix agglomerations subjected to a normal traction.

7. References

[1] M.W. Cook, P.K. Bossom. Trends and recent developments in the material manufacture and cutting tool application of polycrystalline diamond and polycrystalline cubic boron nitride. Int. J. Refract. Met. Hard Mater., 18 (2000) 147 –152

[2] M.P. D'Evelyn, T. Taniguchi. Elastic properties of translucent polycrystalline cubic boron nitride as characterized by the dynamic resonance method. Diamond Relat. Mater., 8 (1999) 1522–1526

[3] D. Carolan, P. Alveen, A. Ivanković, N. Murphy. Effect of notch root

radius on fracture toughness of polycrystalline cubic boron nitride. Eng. Fract. Mech., 78 (2011) 2885–2895

[4] D. Carolan, A. Ivanković, N. Murphy. Thermal shock resistance of polycrystalline cubic boron nitride. J. Eur. Ceram. Soc., 32 (2012) 2581–2586

[5] J.J. Friel, J.C. Grande, D. Hetzner, K. Kurzydlowski, D. Laferty, M.T. Shehata, V. Smolej, G.F. Van-der Voort, L. Wojnar. Practical Guide to Image Analysis. ASM International, 2000.

[6] J.C. Russ. The Image Processing Handbook. CRC Press, 2nd edition, 1995.

[7] W.S. Rasband. ImageJ. U.S. National Institute of Health, Bethesda, Maryland, USA, http://imagej.nih.gov/ij/, 1997–2012

[8] MATLAB. Image Processing Toolbox. The MathWorks Inc., Natick, Massachusetts

[9] M. Groeber, S. Ghosh, M.D. Uchic, D.M. Dimiduk. A framework for automated analysis and simulation of 3D polycrystalline microstructures. Part 2: Synthetic structure generation. Acta Mater. 56:6 (2008)1274–1287

[10] P. Chantikul, S.J. Bennison, B.R. Lawn. Role of Grain Size in the Strength and R-Curve Properties of Alumina. J. Am. Ceram. Soc. 73:8 (1990) 2419–2427

[11] J.P. Singh, A.V. Virkar, D.K. Shetty, R.S. Gordon. Strength-Grain Size

Relations in Polycrystalline Ceramics. J. Am. Ceram. Soc. 62:3-4 (1978) 179–183

[12] R.F. Cook, B.R. Lawn, C.J. Fairbanks. Microstructure-Strength Properties in Ceramics; I, Effect of Crack Size on Toughness. J. Am. Ceram. Soc. 68:11 (1985) 604–615

[13] P. Zhang, D. Balint, J. Lin, Controlled Poisson Voronoi tessellation for virtual grain structure generation: a statistical evaluation. Philos. Mag. 91:36 (2011) 4555–4573

[14] S.A. Langer, E.R. Fuller Jr., W.C. Carter. OOF: An Image-Based Finite-Element Analysis of Materials Microstructures. Comput. Sci. Eng., May/June (2001) 15–23

[15] A.C.E. Reid, S.A. Langer, R.C. Lua, V.R. Coffman, S. Haan, R.E. García. Image-based finite element mesh construction for material microstructures. Comput. Mater. Sci., 43:4 (2008) 989–999

[16] M. Huang, Y. Li. X-ray tomography image-based reconstruction of microstructural finite element mesh models for heterogeneous materials. Comput. Mater. Sci., 67 (2012) 63–72

[17] V.R. Coffman, A.C.E. Reid, S.A. Langer, G. Dogan. OOF3D: An image-based finite element solver for materials science. Math. Comput. Simul. (2012) (http://dx.doi.org/10.1016/j.matcom.2012.03.003)

[18] L. Madej, L. Rauch, K. Perzynski, P. Cybulka. Digital Material Representation as an efficient tool for strain inhomogeneities analysis at the

micro scale level. Archives of Civil and mechanical Engineering, XI(3) (2011) 661–679

[19] P. Zhang, M. Karimpour, D. Balint, J. Lin, D. Farrugia. A controlled Poisson Voronoi tessellation for grain and cohesive boundary generation applied to crystal plasticity analysis. Comput. Mater. Sci., March (2012) 2–7

[20] R. Dobosz, M. Lewandowska, K.J. Kurzydlowski. FEM modelling of the combined effect of grain boundaries and second phase particles on the flow stress of nanocrystalline metals. Comput. Mater. Sci., 53:1 (2012) 286–293

[21] M. Nygårds, P. Gudmundson. Three-dimensional periodic Voronoi grain models and micromechanical FE-simulations of a two- phase steel. Comput. Mater. Sci., 24 (2002) 513–519

[22] M. Kühn, M.O. Steinhauser. Modeling and simulation of microstructures using power diagrams: Proof of the concept. Appl. Phys. Lett., 93 (2008) 034102

[23] H.D. Espinosa, P.D. Zavattieri. A grain level model for the study of failure initiation and evolution in polycrystalline brittle materials. Part I: Theory and numerical implementation. Mech. Mater., 35 (2003) 333–364

[24] D.H. Warner, J.F. Molinari. Micromechanical finite element modeling of compressive fracture in confined alumina ceramic. Acta Mater., 54:19 (2006) 5135–5145

[25] T. Zhou, C. Huang, H. Liu, J. Wang, B. Zou, H Zhu. Crack propagation simulation in microstructure of ceramic tool materials. Comput. Mater. Sci., 54 (2012) 150–156

[26] M. Danielsson, D.M. Parks, M.C. Boyce. Micromechanics, macromechanics and constitutive modeling of the elasto-viscoplastic deformation of rubber-toughened glassy polymers. J. Mech. Phys. Solids, 55:3 (2007) 533–561

[27] P Zhang, D Balint, J Lin. An integrated scheme for crystal plasticity analysis: Virtual grain structure generation. Comput. Mater. Sci., 50 (2011) 2854–2864

[28] D.M. Saylor, J. Fridy, B.S. El-Dasher, K. Jung, A.D. Rollett. Statistically Representative Three-Dimensional Microstructures Based on Orthogonal Observation Sections. Metall. Mater. Trans. A. 35 (2004) 1969–2004

[29] H. Li, K. Li, G. Subhash, L.J. Kecskes, R.J. Dowding. Micromechanical modeling of tungsten-based bulk metallic glass matrix composites. Mater. Sci. Eng., A, 429 (2006) 115–123

[30] Y. Wang, L. Shuhua, P. Xiao, J. Zou. FEM simulations of tensile deformation and fracture analysis for CuW alloys at mesoscopic level. Comput. Mater. Sci., 50 (2011) 3450–3454

[31] H. Digabel, C. Lantuéjoul. Iterative Algorithms. Actes du Second Symposium Europen dAnalyse Quantitative des Microstructur et en Sciences des Matriaux , Biologie et Mdecine, (1978) 85–99

[32] S. Beucher, C. Lantuéjoul. Use of Watershed in Contour Detection. Proc. Int. Workshop Image Proc, (1979) 121–139

[33] L. Vincent, P. Soille. Watersheds in Digital Spaces : An Efficient Algorithm Based on Immersion Simulations. IEEE transactions on pattern analysis and machine intelligence, 13:6 (1991) 583–598

[34] L Vincent. Morphological Gray scale Reconstruction in Image Analysis: Applications and Efficient Algorithms. IEEE transactions on image processing, 2:2 (1993) 176–201

[35] R.C. Gonzalez, R.E. Woods, S.L. Eddins. Digital image processing: using MATLAB. Prentice Hall, 2004.

[36] H.E. Exner, H.P. Hougardy. Quantitative image analysis of microstructures: a practical guide to techniques, instrumentation and assessment of materials. DGM Informationsgesellschaft Verlag, 2nd edition, 1988

[37] Haralick, Shapiro. Computer and Robot Vision, volume 1. Addison-Wesley, 1992

[38] J. L. Bentley. Multidimensional binary search trees used for associative searching. Communications of the ACM, 18:9 (1975) 509–517

[39] H. Weller, G. Tabor, H. Jasak, C. Fureby. A tensorial approach to CFD using object oriented techniques. Computers in Physics, 12 (1998) 620–631

[40] Z. Hashin, S. Shtrikman. A variational approach to the theory of the

elastic behaviour of multiphase materials. J. Mech. Phys. Solids, 11 (1963) 127–140

[41] P. Wall. A comparison of homogenization, Hashin-Shtrikman bounds and the Halpin-Tsai equation. Applications of Mathematics, 42 (1997) 245–257

[42] Z. Hashin. On elastic behaviour of fibre reinforced materials of arbitrary transverse phase geometry. J. Mech. Phys. Solids, 13 (1965)119–134

[43] G. P. Tandon and G. J. Weng. Average stress in the matrix and effective moduli of randomly oriented composites. Compos. Sci. Technol., 27 (1986) 111–132

[44] T. Mori and K. Tanaka. Average stress in matrix and average elastic energy of materials with misfitting inclusions. Acta Metall., 21 (1973) 571– 574

[45] J.D. Eshelby. The determination of the elastic field of an ellipsoidal inclusion, and related problems. Proc. R. Soc. London, Ser. A, 241 (1957) 376–396

[46] X. Chen, Y. Mai. Micromechanics of rubbertoughened polymers. J. Mater. Sci., 33 (1998) 3529–3539

[47] D. Carolan, Mechanical and fracture properties of polycrystalline cubic boron nitride as a function of rate and temperature, PhD Thesis, University College Dublin, 2011